



## Theoretical analysis of graphene plasmon cavities

Xiaofei Xiao<sup>a,\*</sup>, Xiaofeng Li<sup>b</sup>, Joshua D. Caldwell<sup>c</sup>, Stefan A. Maier<sup>a,d</sup>, Vincenzo Giannini<sup>a,e</sup>

<sup>a</sup> The Blackett Laboratory, Imperial College London, London SW7 2AZ, United Kingdom

<sup>b</sup> College of Physics, Optoelectronics and Energy, Collaborative Innovation Center of Suzhou Nano Science and Technology, Key Lab of Modern Optical Technologies of Education Ministry of China, Soochow University, Suzhou 215006, China

<sup>c</sup> Department of Mechanical Engineering, Vanderbilt University, Nashville, TN 37212, United States

<sup>d</sup> Chair in Hybrid Nanosystems, Nanoinstitut München, Faculty of Physics, Ludwig-Maximilians-Universität München, 80799 München, Germany

<sup>e</sup> Instituto de Estructura de la Materia (IEM-CSIC), Consejo Superior de Investigaciones Científicas, Serrano 121, 28006 Madrid, Spain

### ARTICLE INFO

#### Article history:

Received 10 April 2018

Received in revised form 11 June 2018

Accepted 24 June 2018

#### Keywords:

Graphene

Plasmonics

Silicon carbide

Surface phonon polaritons

Sensing

Metamaterials

### ABSTRACT

Unprecedented physical properties make graphene a very promising plasmonic candidate material from the terahertz to mid-infrared frequencies. However, a theoretical model for graphene plasmon cavities has not been fully established. In this work, we analyse the graphene surface plasmon polaritons supported on silicon carbide or metallic cavities. We derive an analytical expression for the dispersion relation of graphene plasmon waves in a multilayer system, providing a useful tool to illustrate the dependence on the cavity's geometric properties. The results show that the analytical description can precisely predict the excitation of cavity graphene plasmon waves. Complete absorption can be achieved under certain parameters, which can be predicted precisely using two Fabry–Pérot models. We further show that the interaction of surface plasmon polaritons with surface phonon polaritons can be used to tune the cavity resonances. The tunability of the Fermi energy and the geometric parameters of the cavities make for flexible system design. High enhancement ( $\sim 4000$ ) and extraordinary compression ( $\sim \lambda_0/400$ ) of graphene plasmon waves are also realized under certain conditions. These findings make this an ideal setup for molecular sensing, pushing the potential for enhanced, broadly tunable spectroscopy into the mid-infrared, while also offering distinct advantages for integrated optics.

© 2018 Elsevier Ltd. All rights reserved.

### 1. Introduction

Surface plasmon polaritons (SPPs) arise due to collective oscillations of free charge carriers in conductors [1,2] and have attracted significant interest for overcoming the diffraction limit [3–5]. Since graphene was experimentally demonstrated in reference [6], it has formed one of the most active areas of research in nanoscience and related technologies due to its unprecedented physical properties [7–9]. In particular, it constitutes a promising two-dimensional (2D) plasmonic material for terahertz (THz) to mid-infrared (MIR) applications [7,10–15]. Compared to the noble metals, graphene has a low carrier concentration, and graphene plasmons (GPs) are thus relatively long-lived and exist at low frequencies [16–19], while the 2D nature of this material leads to highly confined GPs with short wavelengths [20–22]. In addition, the carrier concentra-

tion may be precisely controlled by electrical gating and/or surface doping to permit the existence of GPs along the sheet [10,17].

Despite these impressive advantages, efficiently exciting such plasmonic waves is still challenging due to the large momentum mismatch between the incident light and GPs. Grating coupling [23,24] (where GPs are excited by diffraction effects owing to the grating periodicity), cavity coupling [25,26] (where light scatters off cavity ridges to excite localised modes), near-field coupling [27–30], and excitation by scattering from random structures [31] are widely used schemes to achieve phase matching. Among these, grating coupling and cavity coupling are particularly convenient because as well as assisting the coupling between SPPs and incident light, these structures also can be used as a gate electrode to tune the resonance frequency over a wide spectral range, thereby allowing the system to act as a very tunable optical filter.

Assuming that interband transitions can be ignored, the dispersion relation of the plasmon waves is given by [10,20,23,26]

$$k_{spp}(\omega) = \frac{\pi \hbar^2 \epsilon_0 (\epsilon_1 + \epsilon_2)}{e^2 E_F} \left( 1 + \frac{i}{\omega \tau} \right) \omega^2, \quad (1)$$

\* Corresponding author.

E-mail address: [xiaofei.xiao15@imperial.ac.uk](mailto:xiaofei.xiao15@imperial.ac.uk) (X. Xiao).

URL: <http://www.gianninilab.com> (V. Giannini).

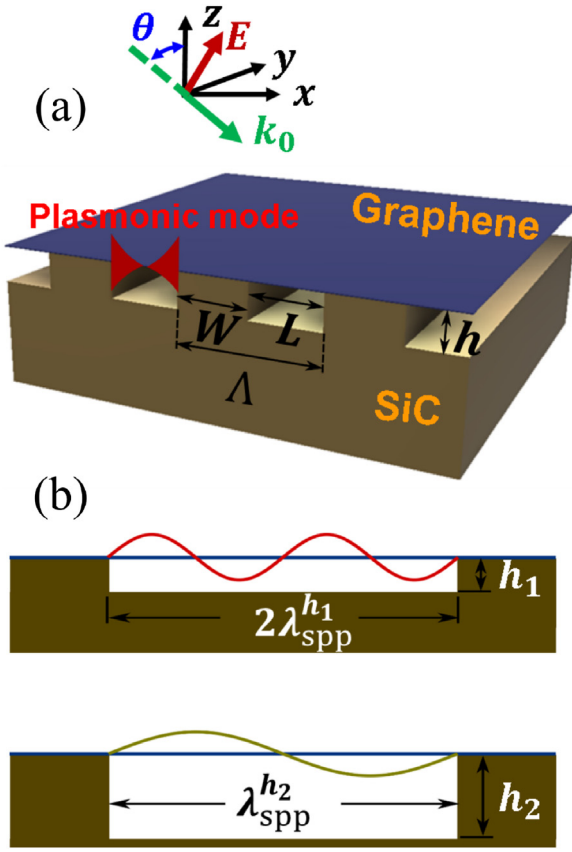


**Fig. 1.** (a) Schematic of a SiC grating-cavity-assisted GP excitation. The incident light is transverse magnetic polarized in air, where  $\Lambda$ ,  $W$ ,  $L$ , and  $h$  are the period, ridge width, trench length, and height of the grating, and  $\theta$  is the incident angle. (b) Sketch of the standing waves of GP resonances with height dependence.

where  $k_{spp}$  is the in-plane wavevector of the plasmon,  $\hbar$  is the reduced Planck constant,  $\epsilon_0$  is the permittivity of free space,  $e$  is the electronic charge,  $E_F = \hbar v_F (\pi n)^{1/2}$  is the Fermi energy measured from the Dirac point,  $v_F \approx 10^6$  m/s is the Fermi velocity in graphene,  $n$  is the sheet carrier density,  $\omega$  is the angular frequency of the wavelength of interest,  $\tau$  is the carrier relaxation time, which is linked to the carrier mobility  $\mu$  via the equation  $\tau = \mu E_F / e v_F$ ,  $\epsilon_1$  and  $\epsilon_2$  are the relative permittivities of the materials in the infinite half-spaces above and below the graphene sheet.

The dispersion relationship of a plasmonic wave in a continuous monolayer of graphene thus depends on the materials above and below the graphene film, as well as the properties of the graphene layer itself. For cavities such as the one shown in Fig. 1a, Eq. (1) predicts the existence of standing waves which have been observed [10,20,23,26]. One important feature of these investigated cavities, however, is that they have very deep ( $>0.5 \mu\text{m}$ ) trenches  $h$ , so that the materials below the cavities have little impact on this relationship. Hence, Eq. (1) provides a good approximation of the behaviour. This is not the case for a shallow cavity. Here, we explore the dependence of the dispersion relationship on the height of the cavity in such systems.

Surface phonon polaritons (SPhPs), similar to SPPs, result from the coupling of the electromagnetic field to the collective lattice vibrations of polar dielectrics at infrared frequencies [2,32]. Silicon carbide (SiC) is an exemplary polar dielectric supporting sub-diffraction confinement of light via the excitation of SPhP modes [33–37]. Because of the energy scale of optical phonons, such SPhP modes can be stimulated within this spectral range, referred to as the Reststrahlen band, which is bound by the longitudinal (LO) and transverse optic (TO) phonon frequencies. In the Reststrahlen

band, polar dielectrics act similarly to an optical metal but with much lower optical losses due to the long phonon scattering lifetime [33] compared to their plasmonic counterparts. More recently, active modulation of the permittivity (and consequently the SPhP resonances) in nanostructured SiC has been realized by using the coupling of photo-injected carriers and optic phonons [38,39], and by using phase change materials [40]. All of these advantages, as well as high thermal, mechanical and chemical stability, make SiC highly suitable for a range of applications in MIR photonics.

In this paper, we explore the dependence of the dispersion relationship on the height of the cavity, and explore the coupling between SPhPs and GPs. We derive an analytical expression for the dispersion relation of the GP waves in a multilayer system, providing a useful tool to show the influence of the materials below the cavity on the dispersion relationship. We consider a system comprising a single layer of graphene and a SiC cavity (see Fig. 1). The scattering from the sharp edges of the cavity overcomes the large mismatch between the GPs and the incident light. The absorption properties and field distributions of this system in the infrared range are investigated using the finite element method (FEM) utilizing COMSOL Multiphysics. The results show that the derived analytical description of the dispersion relation of the GPs can precisely predict the excitation of the cavity GP waves, while Eq. (1) fails for systems with shallow cavities. Additionally, results shows complete absorption can be achieved under certain parameters, which can be predicted precisely using a Fabry–Pérot model in the horizontal direction for GPs and a Fabry–Pérot model in the vertical direction for gap SPhPs. This means that the interaction of the SPPs and SPhPs can be used to tune the cavity resonances. High enhancement and extraordinary compression of GPs are realized under certain conditions. We further provide results for different doping levels and different substrates. Under normal incident excitation, only antisymmetric plasmon modes are excited because of the symmetry of the system. To excite symmetric plasmon modes, we adopt oblique incidence to break the system symmetry. Finally, a potentially simpler and more realistic configuration is outlined.

## 2. Methods

In our calculations, we model the graphene as a 2D continuous sheet characterized by its in-plane electrical conductivity  $\sigma_g$ . Such conductivity can be expressed as  $\sigma_g = \sigma_{intra} + \sigma_{inter}$ , where  $\sigma_{intra}$  and  $\sigma_{inter}$  refer the contributions from the intraband and interband transitions of electrons in graphene, respectively. Within the local random-phase approximation model [7,41,42], they are given by [14]

$$\sigma_{intra} = \frac{2ie^2 k_B T}{\pi \hbar^2 (\omega + i/\tau)} \ln \left[ 2 \cosh \left( \frac{E_F}{2k_B T} \right) \right], \quad (2)$$

and

$$\sigma_{inter} = \frac{e^2}{4\hbar} \left[ \frac{1}{2} + \frac{1}{\pi} \arctan \left( \frac{\hbar\omega - 2E_F}{2k_B T} \right) - \frac{i}{2\pi} \ln \left( \frac{(\hbar\omega + 2E_F)^2}{(\hbar\omega - 2E_F)^2 + (2k_B T)^2} \right) \right], \quad (3)$$

where  $k_B$  is the Boltzmann constant,  $T$  is the temperature, and all other symbols have their usual meaning. In our calculations,  $T = 300$  K and  $\mu = 10,000$  cm<sup>2</sup>/(Vs) (thus,  $E_F = 0.64$  eV) are used. In Fig. 2b we plot the conductivity of graphene under different doping conditions at MIR wavelengths.

For polar dielectrics, the dielectric function employing a Lorentz oscillator model reads

$$\epsilon(\omega) = \epsilon_\infty \left( 1 + \frac{\omega_{LO}^2 - \omega_{TO}^2}{\omega_{TO}^2 - \omega^2 - i\omega\gamma} \right), \quad (4)$$

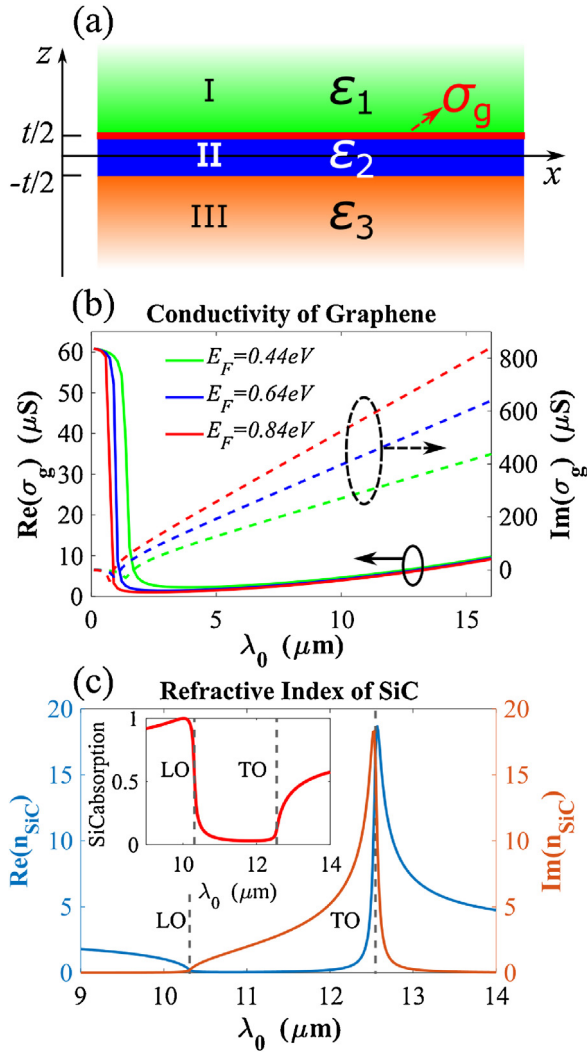


**Fig. 2.** (a) Geometry of a three-layer system consisting of a thin layer II sandwiched between two infinite half spaces I and III with an interface between media I and II characterized by a complex surface conductivity  $\sigma_g$  (representing graphene or, more generally, any conducting 2D material). (b) Real (solid) and imaginary (dashed) parts of the conductivity of graphene in air under different doping conditions. (c) Real and imaginary parts of the refractive index of bulk SiC around its Reststrahlen band, which is bound by the LO and TO phonon frequencies. The inset shows the absorption of a plain SiC substrate.

which has a pole at the TO phonon frequency  $\omega_{TO}$  and a zero-point crossing at  $\omega_{LO}$ . Fig. 2c shows the refractive index (the absorption is given in the inset) of SiC [43] for  $\epsilon_\infty = 6.56$ ,  $\omega_{LO} = 969.9 \text{ cm}^{-1}$ ,  $\omega_{TO} = 797 \text{ cm}^{-1}$  and  $\gamma = 4.76 \text{ cm}^{-1}$ .

### 3. Results and discussion

This section is structured as follows: in Section 3.1, we derive the dispersion relation for the GP waves in multilayer systems. In Section 3.2, we excite the standing waves using the Fabry–Pérot cavity effect in the horizontal direction, compare the predictions from the derived dispersion relation and the simulation results using FEM, and discuss the influence of the materials below the cavity on the dispersion relationship. In Section 3.3, we explore the cavity height-dependence of GPs, present the vertical Fabry–Pérot cavity effect, and discuss the coupling between SPhPs and SPPs in this system. In Section 3.4, we further report the high enhancement and extraordinary compression of the GPs. In Section 3.5, we present examples under different doping levels. In Section 3.6, we demonstrate the

possibility of exciting symmetric plasmon modes at oblique incidence. In Section 3.7, we compare the effects of different substrates. In Section 3.8, we outline the potentially simpler and more realistic configuration.

#### 3.1. Graphene plasmons in multilayer systems

We consider the most general three-layer system consisting of alternating conducting and/or dielectric films with non-source-free boundary conditions, as illustrated in Fig. 2a: Firstly, layer II, a slab of thickness  $t$ , is sandwiched between two infinitely thick claddings (layers I and III). The relative permittivities and permeabilities are  $\epsilon_i$  and  $\mu_i$ , respectively, where  $i = 1, 2, 3$  represent materials I, II and III, respectively, and  $\mu_i$  is equal to 1 for non-magnetic materials. Secondly, a complex surface conductivity  $\sigma_g$  is used to describe the property of the interface between media I and II. Hence, one can identify it as a I-G-II-III system, where I, II and III represent metal or dielectric materials, and G represents a 2D material (graphene in this example). In such a system, each single interface may sustain bound SPPs or SPhPs depending on the configuration. It is worth noting that previously studied metal-insulator-metal structures, insulator-metal-insulator structures, insulator-excitonic material-insulator structures, and insulator-insulator-insulator structures including 2D materials can be regarded as special cases of this system [2,44,45].

Since we are only interested in the lowest-order GP modes here, we begin by looking for the general transverse magnetic (TM) solution. Using the coordinate system of Fig. 2a, we write the wavenumber of GPs as  $\beta$ , which corresponds to the component of the wavevector in the direction of propagation ( $x$ -direction). In source-free regions of space, the GP magnetic fields and electric fields can be expressed by the following sets of equations

$$H_y = \begin{cases} Ae^{i\beta x} e^{-k_1 z} & (z > t/2) \\ Ce^{i\beta x} e^{k_2 z} + De^{i\beta x} e^{-k_2 z} & (-t/2 < z < t/2) \\ Be^{i\beta x} e^{k_3 z} & (z < -t/2) \end{cases}, \quad (5a)$$

$$E_x = \begin{cases} iA \frac{1}{\omega \epsilon_0 \epsilon_1} k_1 e^{i\beta x} e^{-k_1 z} & (z > t/2) \\ -iC \frac{1}{\omega \epsilon_0 \epsilon_2} k_2 e^{i\beta x} e^{k_2 z} + iD \frac{1}{\omega \epsilon_0 \epsilon_2} k_2 e^{i\beta x} e^{-k_2 z} & (-t/2 < z < t/2) \\ -iB \frac{1}{\omega \epsilon_0 \epsilon_3} k_3 e^{i\beta x} e^{k_3 z} & (z < -t/2) \end{cases}, \quad (5b)$$

$$E_z = \begin{cases} -A \frac{\beta}{\omega \epsilon_0 \epsilon_1} e^{i\beta x} e^{-k_1 z} & (z > t/2) \\ C \frac{\beta}{\omega \epsilon_0 \epsilon_2} e^{i\beta x} e^{k_2 z} + D \frac{\beta}{\omega \epsilon_0 \epsilon_2} e^{i\beta x} e^{-k_2 z} & (-t/2 < z < t/2) \\ -B \frac{\beta}{\omega \epsilon_0 \epsilon_3} e^{i\beta x} e^{k_3 z} & (z < -t/2) \end{cases}, \quad (5c)$$

where  $k_0$  is the wavenumber in free space ( $k_0 = \omega/c = 2\pi/\lambda_0$ ,  $\lambda_0$  is the free-space wavelength,  $c$  is the speed of light in vacuum),  $A$ ,  $B$ ,  $C$  and  $D$  are the field amplitudes satisfying the boundary conditions,  $k_i \equiv k_{i,z}$ , denotes the  $z$ -components of the wavevectors in the three materials, which reads  $k_i^2 = \beta^2 - k_0^2 \epsilon_i$  for  $i = 1, 2, 3$ .

By applying the boundary conditions, the following requirements should be satisfied at the interfaces between non-magnetic materials

$$\begin{cases} E_x^1 = E_x^2, & H_y^1 - H_y^2 = -\sigma_g E_x^2 & \text{at } z = t/2 \\ E_x^2 = E_x^3, & H_y^2 = H_y^3 & \text{at } z = -t/2 \end{cases}. \quad (6)$$

Solving this system of linear equations results in an implicit expression for the dispersion relation linking  $\beta$ ,  $t$ , and  $\omega$  via

$$e^{-2k_2 t} = \frac{k_2/\epsilon_2 \delta + k_1/\epsilon_1 k_2/\epsilon_2 + k_3/\epsilon_3}{k_2/\epsilon_2 \delta - k_1/\epsilon_1 k_2/\epsilon_2 - k_3/\epsilon_3}, \quad (7)$$

where

$$\delta = 1 + \frac{i\sigma_g}{\omega\epsilon_0\epsilon_1} k_1. \quad (8)$$

The impact of the material not in contact with the graphene layer is fully considered in the derived dispersion relation, which will show a significant distinction for shallow cavity assisted structures. It should be noted that Eq. (7) is valid for both real and complex  $\epsilon_i$ . The considered system represents a variety of configurations under some assumptions, such as  $\sigma_g = 0$ . Additionally, this expression implies that  $\beta$  cannot be written in an explicit form. We note that when  $t$  is large enough, Eq. (1) is a good approximation of Eq. (7). Finally, the GP magnetic and electric fields are obtained from Eqs. (5a–5c)

$$\begin{cases} A = D \frac{2k_1/\epsilon_1 \delta}{k_1/\epsilon_1 \delta + k_3/\epsilon_3} e^{(k_3 - k_1)t/2} \\ B = D \left[ \frac{k_1/\epsilon_1 \delta - k_3/\epsilon_3}{k_1/\epsilon_1 \delta + k_3/\epsilon_3} e^{(k_2 - 3k_1)t/2} + e^{(k_1 + k_2)t/2} \right] \\ C = D \frac{k_1/\epsilon_1 \delta - k_3/\epsilon_3}{k_1/\epsilon_1 \delta + k_3/\epsilon_3} e^{-k_1 t} \end{cases}. \quad (9)$$

The in-plane wavevector of the GP,  $\beta$ , is a complex number with the real and imaginary parts determining the GP wavelength,  $\lambda_{spp} = 2\pi/\text{Re}\{\beta\}$ , and the propagation length,  $L_{spp} = 1/(2 \cdot \text{Im}\{\beta\})$ . To investigate the properties of GPs, the effective refractive index (ERI) of the GP defined by the following equation is used

$$N_{eff} = \frac{\beta}{k_0}. \quad (10)$$

In the following section,  $\beta$  will be written as  $k_{spp}^h$  (where  $k_{spp}^h = N_{eff} k_0$ ) to explicitly show the height dependence of the wavevector of the GPs. We should bear in mind that in most cases, we expect strong field confinement and long propagation length.

### 3.2. Graphene plasmon cavity

The plasmonic waves in graphene have extremely high field confinement, which enable us to build devices with dimensions well beyond the diffraction limit. However, to excite the GPs with a free-space optical wave is still very challenging due to the large differences in wavevector. Here we use one of the most widely used schemes – scattering from the sharp edges of cavities, as shown in Fig. 1a, to provide the necessary additional momentum and efficiently facilitate the excitation, whilst we consider the cavity as part of a periodic structure (i.e. a grating that is convenient for experiments and numerical simulations). It is worthwhile noting that scattering by defects (sharp ridges, in our case) generates a broad spectrum of wavevectors, in which a solution to the following coupling condition can be easily found

$$k_{spp}^h(\lambda_0) = \frac{2\pi}{\lambda_0} \sin(\theta) + K. \quad (11)$$

Here  $k_{spp}^h$  is the wavevector of the GPs,  $\theta$  is the incident angle, and  $K$  is the compensated wavevector generated from the scattering process. The superscript  $h$  is explicitly used to stress the dependence of the dispersion relationship on the height of the cavity in Fig. 1a. For a normal incident wave ( $\theta = 0^\circ$ ),  $k_{spp}^h(\lambda_0) = K$ .

Although the wavevector mismatch is overcome by scattering, the condition for establishing standing waves in the cavity needs to be satisfied, because GPs are excited from both edges and the

forward and backward launched waves must constructively interfere. The cavity length  $L$  needed for free-space wavelength  $\lambda_0$  is determined by a Fabry–Pérot equation

$$\delta\phi + \Re(k_{spp}^h(\lambda_0)L) = m\pi, \quad m = 0, 1, 2, 3, \dots, \quad (12)$$

where  $\delta\phi$  is the phase shift and the integer  $m$  denotes the resonance mode order. In this paper, the tangential component of the electric field at the edges needs to vanish as a consequence of the electric field boundary conditions, resulting in a phase shift of  $-\pi$  for the plasmon waves. Fig. 1b shows the height-dependent standing waves of the GPs supported on the cavity.

For a TM wave, the plasmonic waves in graphene are excited when the cavity length  $L$  matches Eq. (12) and the optical energy is dissipated due to the Ohmic loss while the plasmonic wave propagates in the graphene monolayer. At normal incidence, the GP waves originated from the two edges of the cavity are out-of-phase, and thus, antisymmetric plasmon modes associated with odd-mode order in Eq. (12) can occur. At oblique incidence, the in-phase plasmons can be excited from two edges, and thus, the plasmons with even-mode order can be excited. Here we simulate the optical response of the structure shown in Fig. 1 using FEM. Unless specified, the incident light is TM polarized and incident from the air side, normal to the surface. Our study [26] shows that the ridge width does not change the essence of the proposed theory used to precisely predict the excitation of cavity GP waves, and that the ridge width does have influence on the excitation efficiency of the graphene absorption. To obtain a high efficiency for this work, we have fixed the ridge width at  $2 \mu\text{m}$ .

To validate our theory we begin by considering the short grating height case. In the simulation, incident wavelengths and cavity lengths are in the range  $10 \mu\text{m} \rightarrow 13 \mu\text{m}$  and  $0.1 \mu\text{m} \rightarrow 2.5 \mu\text{m}$ , respectively, with a grating height fixed at  $0.15 \mu\text{m}$ . The SiC substrate is infinitely thick below the grating to switch off the transmission channel and simplify the analysis. Fig. 3a shows the ERI for different values of the incident wavelength  $\lambda_0$  obtained from Eq. (7), where media I and II are air, and medium III is SiC (in Fig. 2a). One striking feature is the abrupt change of the ERI with incident wavelength around  $10.5 \mu\text{m}$ . This can be understood by noting the change of the refractive index of SiC. It can be seen that real and imaginary parts of ERI decrease dramatically at first and then slowly with increasing incident wavelength, when  $\lambda_0 > 10.5 \mu\text{m}$ . The ERI obtained from Eq. (1) is also shown in Fig. 3a (solid lines). The difference between these two results shows the essential distinction between the calculations with and without considering the influence of the material below the cavity.

We calculate the whole absorption ( $P_{abs}^W$ , representing the sum of the absorption of the SiC grating and the graphene layer) of a SiC grating with graphene sheet present versus the trench length ( $L$ ) and the incident wavelength ( $\lambda_0$ ) shown in Fig. 3b, when  $W = 2 \mu\text{m}$ ,  $h = 0.15 \mu\text{m}$ . The strong absorption peaks around the SiC LO frequency are mainly due to the excitation of SPhPs in the SiC grating [26]. Graphene layer absorption ( $P_{abs}^G$ ) in the SiC grating plus graphene structure is also shown in Fig. 3c. The appearance of the absorption peaks in the low absorption region of the Reststrahlen band for certain cavity lengths, shown in Fig. 3b and c, is evidence of the excitation of the GP. The electromagnetic field is concentrated on the graphene layer and the plasmon modes are antisymmetric plasmon standing waves at normal incidence. These findings have similarities with published work on the excitation of GP modes using a grating or cavity [25,26]. However, because the cavities used in those works are very deep, Eq. (1) is sufficient to predict the peak positions for these systems. To show how Eqs. (7) and (1) contrast, both equations are used to theoretically predict the absorption peak positions in our system, as shown in Fig. 3c. The remarkable agreement between the results from Eq. (7) (compared with the ones from Eq. (1), indicated by the black dashed

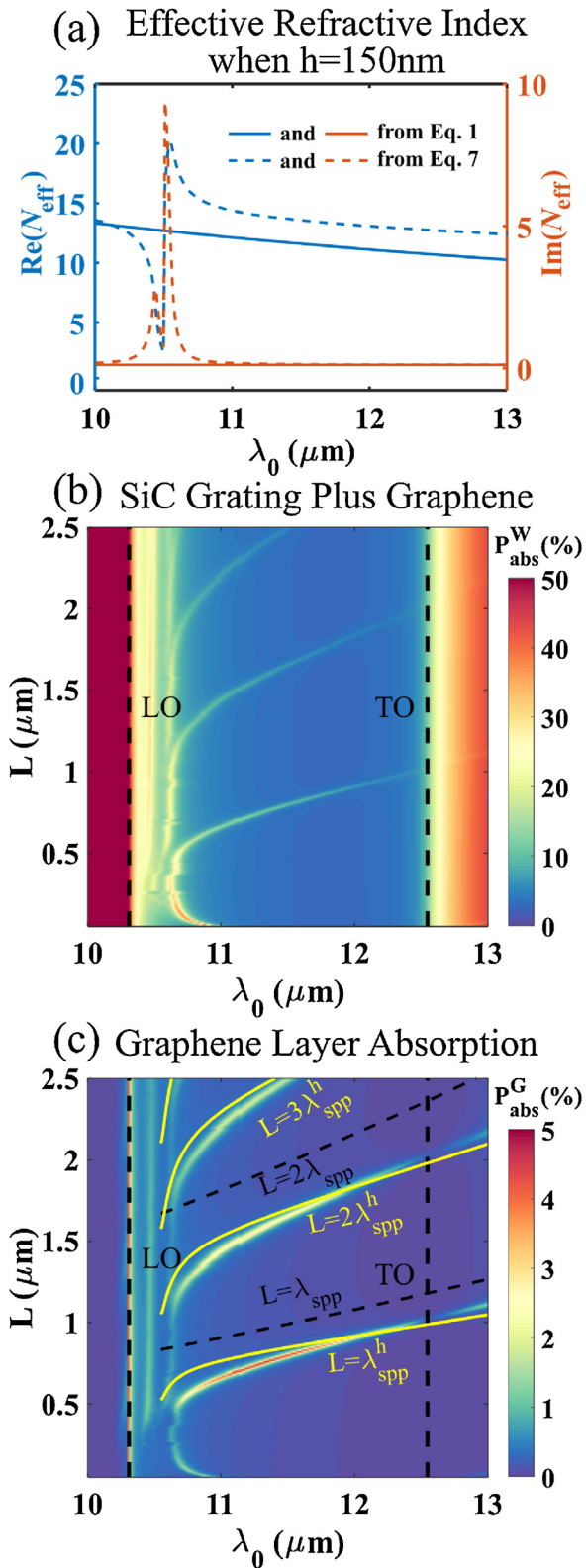


**Fig. 3.** (a) Real and imaginary parts of the ERI for different values of the incident wavelength  $\lambda_0$  obtained from both Eqs. (7) and (1), where media I and II are air, medium III is SiC,  $E_f = 0.64$  eV, and  $h = 0.15$   $\mu\text{m}$ . (b) Under TM polarized normal incident light, whole absorption ( $P_{\text{abs}}^W$ ) for the SiC grating plus graphene structure versus the trench length ( $L$ ) and the incident wavelength ( $\lambda_0$ ), when  $W = 2\mu\text{m}$ , and  $h = 0.15$   $\mu\text{m}$ . (c) Graphene layer absorption ( $P_{\text{abs}}^G$ ) for the same structure used in (b). The yellow and black curves indicate a fit to a Fabry–Pérot model for a phase shift of  $-\pi$  (see Eq. (12)) using Eqs. (7) and (1), respectively.

curves) and the ones from the numerical simulation indicates that: (i) the material below the cavity has a distinct influence on the dispersion relationship of the plasmonic wave on the graphene layer when the cavity is shallow, and (ii) the localized cavity modes are excited by the scattering from the cavity edge rather than by diffraction effects owing to the grating periodicity [26,46], since the peak position does not change with varying  $\Lambda$  (for a fixed cavity length, see reference [26] for more details).

To reveal the mechanism of the cavity height dependence of the dispersion relationship in our system, we investigate the system by varying the cavity height for a fixed wavelength  $\lambda_0 = 12$   $\mu\text{m}$ , as shown in Fig. 4. The ERI against the grating height is calculated using Eq. (7) shown in Fig. 4a. We find that the real and imaginary parts of the ERI begin to drop drastically until the height reaches 0.3  $\mu\text{m}$ . After  $h$  exceeds sizes larger than 0.5  $\mu\text{m}$ , the difference between the ERIs calculated from different equations is negligible. This is because when  $h$  is large ( $h > 0.5$   $\mu\text{m}$  here), Eq. (1) is a good approximation of Eq. (7), which means now  $k_{\text{spp}}^h$  depends only on the material directly above and below the suspended graphene (in this case, air). These findings are demonstrated more clearly by the good agreement between the analytical results from Eq. (7) and those from the FEM simulations for the SiC grating plus graphene structure as shown in Fig. 4b. The field distribution for different peaks shows that antisymmetric modes are excited. We emphasize again the dependence of  $\lambda_{\text{spp}}^h$  on the cavity height, in contrast to previous works. In Fig. 4c and d, we plot the near-fields for two systems with the same geometry, with the only exception being the different cavity heights ( $h = 0.032$   $\mu\text{m}$  and  $h = 0.284$   $\mu\text{m}$ ), showing that we are able to excite two different modes by only varying the cavity height. This is pictorially shown in Fig. 1b. We also show the near-field distribution for another pair of systems with the same geometry, except for differences in the trench length ( $L = 1.03$   $\mu\text{m}$  and  $L = 2.07$   $\mu\text{m}$ ) in Fig. 4d and e. These findings enable us to tune the cavity resonances by varying the geometric parameters. Specifically, the cavity height can be used to tune the wavelength of the plasmonic waves on the graphene. The tunability of these geometric parameters make this system very versatile.

To further confirm these findings, Fig. 5a shows the graphene absorption varying with cavity length (for a fixed wavelength  $\lambda_0 = 12$   $\mu\text{m}$ ). The peaks at integer multiples of  $L/\lambda_{\text{spp}}^h$  correspond to the standing waves of the GPs as indicated by the near-field distribution plots in Fig. 5b–e. The peak position does not change for different values of the grating period because of the independence of the excitation of the localized cavity modes on the grating effect. Comparison of the predictions from Eqs. (7) and (1) demonstrates that the former provides more accurate results.

### 3.3. Simultaneous excitation of graphene plasmon cavity modes and vertical SiC Fabry–Pérot cavity modes

The above work derives the dispersion relation of GP waves in multilayer systems, confirms the influence of the materials below the cavity on the dispersion relationship, and demonstrates the Fabry–Pérot cavity effect in the horizontal direction. In this part we explore the vertical property of the system. In Fig. 4b, it is worth noting that the absorption is weak ( $< 15\%$ ) when the cavity is very shallow, although becomes stronger as the cavity height  $h$  increases. Considering the fact that in this region of the spectrum SiC acts, to a good approximation, as a perfect electric conductor (PEC), it would seem that Fabry–Pérot resonances could be achieved in the vertical direction of the cavity for certain parameters.

To prove this hypothesis, in Fig. 6a, we investigate the whole absorption of the complete system, the SiC absorption and the graphene absorption varying with the cavity height  $h$  (for a fixed wavelength  $\lambda_0 = 12$   $\mu\text{m}$  and trench length  $L = 1.06$   $\mu\text{m}$ ). Note that all curves in Fig. 6a present stationary periodic oscillation behavior,

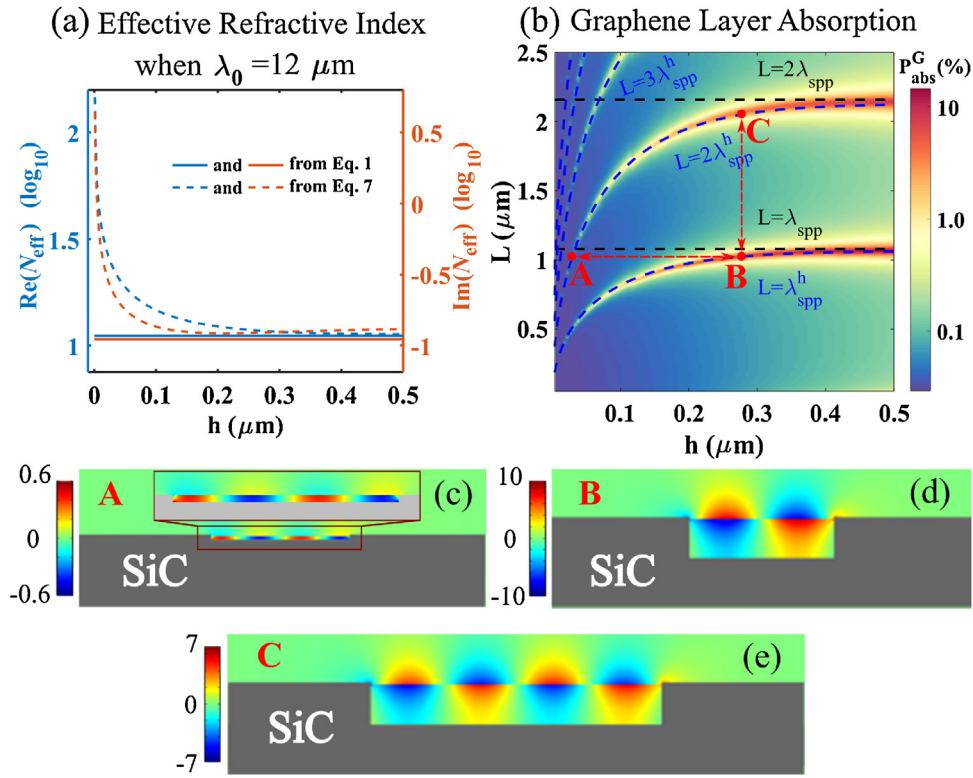


**Fig. 4.** (a) Real and imaginary parts of the ERI from Eqs. (7) and (1) against the grating height ( $h$ ) for TM polarized, normal incidence light at a fixed wavelength  $\lambda_0 = 12 \mu\text{m}$ , where media I and II are air, medium III is SiC, and  $E_F = 0.64 \text{ eV}$ . (b) Graphene layer absorption ( $P_{abs}^G$ ) for the SiC grating plus graphene structure versus the trench length ( $L$ ) and the grating height ( $h$ ). The blue and black curves indicate a fit to a Fabry–Pérot model for a phase shift of  $-\pi$  (see Eq. (12)) when using Eqs. (7) and (1), respectively. (c–e) Near-field distribution of  $E_z$  for three cases marked as points A, B, and C in (b). (c) A second-order mode with  $h = 0.032 \mu\text{m}$  and  $L = 1.03 \mu\text{m}$ . (The zoom-in view is given as well.) (d) A first-order mode with  $h = 0.284 \mu\text{m}$  and  $L = 1.03 \mu\text{m}$ . (e) A second-order mode with  $h = 0.284 \mu\text{m}$  and  $L = 2.07 \mu\text{m}$ . The electric field distribution verifies the height dependence of the standing waves supported on the cavity. The electric field is normalised to the incident field magnitude. Different colorbars are used.

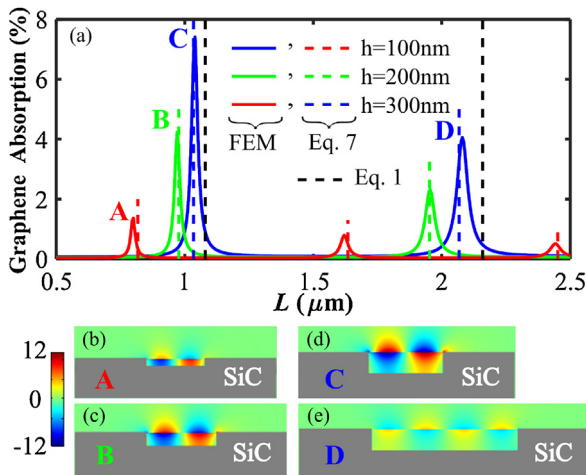


**Fig. 5.** (a) Graphene absorption for different geometric parameters ( $h$  and  $L$ ) of the SiC grating. Predictions of peak positions obtained from Eq. (7) are indicated by the vertical, colored, dashed lines. Predictions from Eq. (1) are also given. (b–e) The peaks correspond to standing waves of the GPs as indicated by the near-field plots of  $E_z$  for peaks A ( $h = 0.1 \mu\text{m}$  and  $L = 0.8 \mu\text{m}$ ), B ( $h = 0.2 \mu\text{m}$  and  $L = 0.97 \mu\text{m}$ ), C ( $h = 0.3 \mu\text{m}$  and  $L = 1.04 \mu\text{m}$ ), and D ( $h = 0.3 \mu\text{m}$  and  $L = 2.04 \mu\text{m}$ ). The electric field goes to zero at the boundaries meaning the plasmon modes must be antisymmetric.

which is also verified by the perfect linear relation of the peak positions shown in Fig. 6b. The period is about  $4.574 \mu\text{m}$ , which equals half of the effective wavelength in the cavity ( $\lambda_0 / \text{Re}\{N_{eff}^{SPhP}\} / 2 = 12 / 1.3131 / 2 = 4.569 \mu\text{m}$ . The definition of  $N_{eff}^{SPhP}$  and details of its calculation will be provided later.). This is understood by noting

that there are SPhP modes excited on the cavity walls as indicated by the electromagnetic fields in Fig. 6c–h. Similar to gap SPPs [47], for sufficiently small gap widths, the SPhPs associated with the two cavity walls interact with each other and form single gap modes, in which the fundamental symmetric eigenmode exhibits an even symmetry of the normal field component,  $E_x$  as shown in Fig. 6c–e, and odd symmetry of the tangential electric field component,  $E_z$  as shown in Fig. 6f–h. Similarly, these gap modes can be termed as gap SPhPs, although they are more accurately described as slot wave-guide modes, having the ability to achieve strong mode confinement together with relatively low Ohmic dissipation. Similar to the wavelength and the propagation length of gap SPPs, the wavelength and the propagation length of gap SPhP are defined as  $\lambda_{SPhP} = 2\pi / \text{Re}\{\beta_{SPhP}\}$  and  $L_{SPhP} = 1 / (2 \cdot \text{Im}\{\beta_{SPhP}\})$ , respectively, where  $\beta_{SPhP} = N_{eff}^{SPhP} \cdot k_0$  is the in-plane wavevector of the gap SPhP and  $N_{eff}^{SPhP}$  is the ERI of the gap SPhP.  $\beta_{SPhP}$  can be calculated using Eq. (7). In our case, we assume that  $\sigma_g = 0 \mu\text{S}$ ,  $t = 1.06 \mu\text{m}$ , medium I and III are SiC, and medium II is air.

The curves in Fig. 6a divide into two parts, as shown by the grey dashed line. When the cavity height is smaller than  $24.95 \mu\text{m}$  (left part in Fig. 6a), it is observed that complete absorption can be achieved in the system for certain cavity heights. This indicates the critical coupling condition is satisfied [48], and a standing wave is formed. This can be understood by noticing that the reflection of the front of the graphene film can be completely cancelled by the leaked wave from the cavity formed by the graphene layer and back mirror (the bottom material). Meanwhile, the graphene absorption (even 72% is achievable) dominates the whole absorption of the system. Fig. 6c–e shows clearly that the standing waves are formed in the vertical direction of the cavity. Thus, the Fabry–Pérot cavity

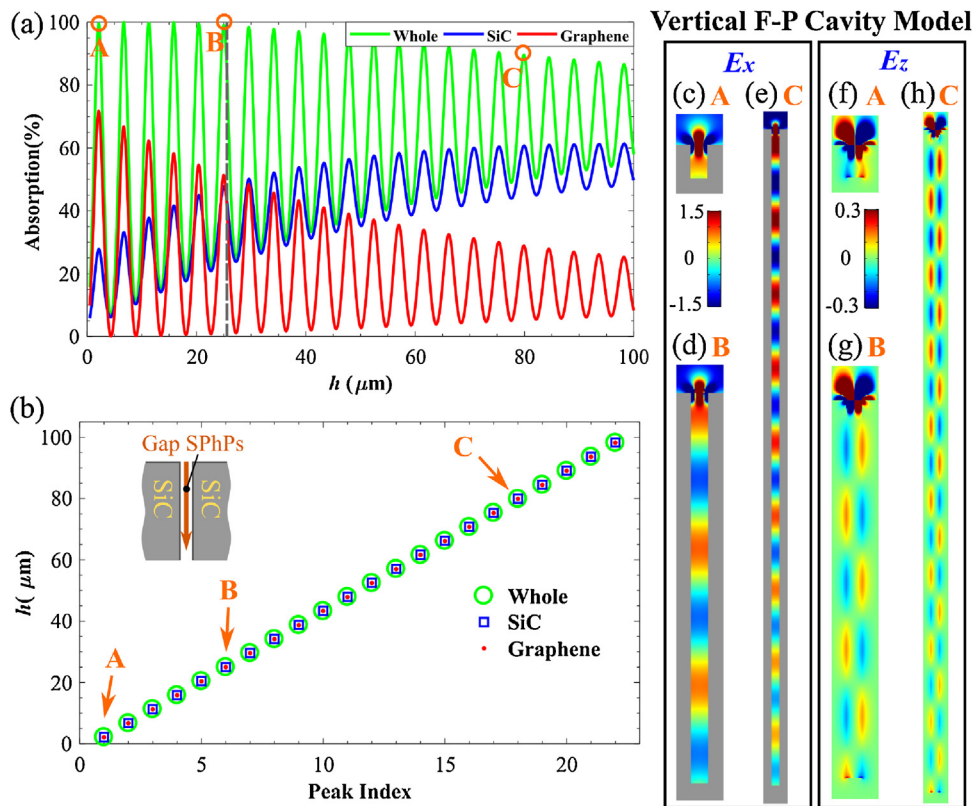


**Fig. 6.** Vertical Fabry–Pérot Cavity Model. (a) Whole absorption, SiC absorption, and graphene layer absorption of the SiC grating plus graphene structure (with  $W = 2 \mu\text{m}$  and  $L = 1.06 \mu\text{m}$ ) as functions of the grating height at incident wavelength of  $\lambda_0 = 12 \mu\text{m}$ . (b) Peak positions of these three types of absorptions. The peak positions for the three types of absorptions coincide. The peaks are periodically spaced as a function of the grating height. The inset shows the schematic of an air slab sandwiched between two infinite half spaces (SiC), which is a special case of the structure in Fig. 2a. Gap SPhPs are generated in this structure. The distributions of x- and z-components of the electric field ( $E_x$  and  $E_z$ , respectively) corresponding to the points marked A, B, and C in (a) and (b) are shown for  $h = 2.13 \mu\text{m}$  (c and f),  $h = 25 \mu\text{m}$  (d and g), and  $h = 79.9 \mu\text{m}$  (e and h). The same colorbar is used for each component, while the scales in (e and h) are half of the ones used in (c), (d), (f), and (g). The peaks correspond to standing waves of the gap SPhPs supported in the vertical direction of the SiC cavity as indicated by the near-field plots of  $E_x$  in (c–e). The fundamental symmetric gap SPhP eigenmode propagating along the z-axis supported by the cavity is clearly seen in (c–h). The gray dashed line in (a) indicates a boundary, after which the graphene absorption is smaller than the SiC absorption.

hypothesis in the vertical direction is verified. When the cavity height is larger than  $24.95 \mu\text{m}$  (right part in Fig. 6a), complete absorption of the system cannot occur, and the SiC absorption becomes the main part of the whole absorption in the system. The increasing SiC absorption is mainly due to the increasing area of the SiC walls in the cavity. Because of the increase of the SiC absorption, the intensity of the reflected waves from the bottom decreases, and thus reduces the excitation efficiency of the plasmonic modes on the graphene. Meanwhile, the reflection of the front of the graphene layer cannot be completely cancelled, and consequently complete absorption cannot be achieved. All three absorptions approach constant values (the constant values of the total system absorption, the SiC absorption and the graphene absorption are about 70%, 55% and 15%, respectively) when the cavity height is significantly (about five times) larger than half the characteristic propagation length of the gap SPhP ( $L_{\text{SPhP}}/2 = 76.4 \mu\text{m}$ ). Because in this case most of the energy of the gap SPhPs is absorbed by the cavity walls. The proposed configuration can achieve an efficient coupling of photons to GPs and gap SPhPs, as well as provide strong coupling between GPs and gap SPhPs, for the development of future devices.

#### 3.4. High enhancement and extraordinary compression of graphene plasmons

In Fig. 7, we show the intensity distributions for two special cases. This figure reveals that the most striking features are the strong intensity (the highest enhancement is  $\sim 4000$  in

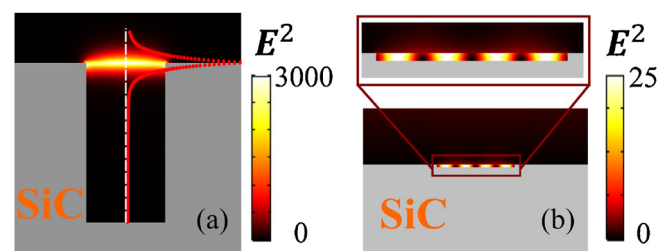


**Fig. 7.** (a) High intensity ( $E^2$ ) distribution for the first complete absorption peak at  $h = 2.13 \mu\text{m}$  and  $L = 1.06 \mu\text{m}$  marked as point A in Fig. 6a. Distribution of the intensity along the gray dashed line at the center of the cavity is given as well. The enhancement around the graphene layer in this case is about 4000. (b) Intensity ( $E^2$ ) distribution of the extraordinary compressed plasmonic waves trapped in the cavity with  $h = 0.032 \mu\text{m}$  and  $L = 1.03 \mu\text{m}$  marked as point A in Fig. 4b. The compression factor of  $\lambda_0/h$  in this case is 375.

Fig. 7a) when the complete absorption in the system occurs, and the extraordinary confinement (the compression factor is 375 in Fig. 7b) of the electromagnetic field. In Fig. 7a, the extremely high field enhancement is compressed on the graphene layer providing high potential for applications in molecular sensors. This is in contrast to the grating system in the aforementioned references [26,46] where the field enhancement is limited. Fig. 7b shows the ability for trapping GPs in an extremely small gap. This confinement can be even stronger when using a much shallower cavity. However, the graphene absorption will get smaller with the reduction of  $h$ ,

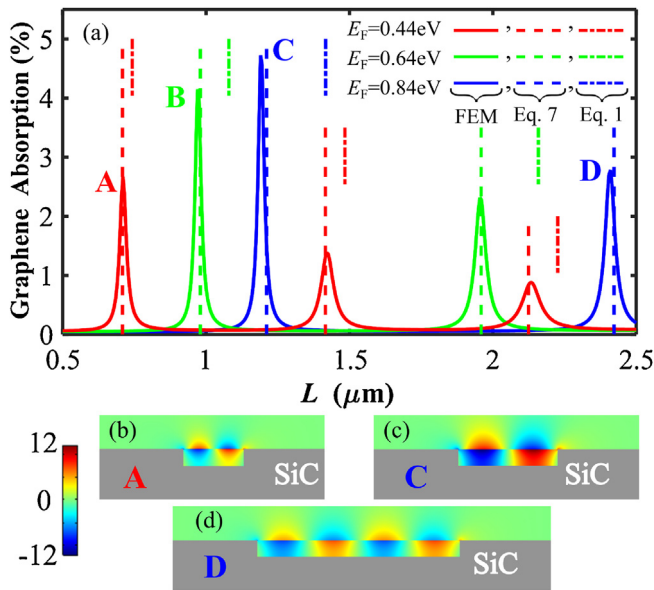


**Fig. 8.** (a) Graphene layer absorption for different Fermi energies ( $E_F$ ) and trench lengths ( $L$ ) of the SiC grating when  $h=0.2\ \mu\text{m}$ ,  $W=2.0\ \mu\text{m}$ , and  $\lambda_0=12\ \mu\text{m}$ . Predictions of peak positions from Eq. (7) are indicated by the vertical, colored, dashed lines. Predictions from Eq. (1) are also given. (b–d) The peaks correspond to standing waves of the GPs as indicated by the near-field plots of  $E_z$  for peaks A ( $E_F=0.44\ \text{eV}$  and  $L=0.71\ \mu\text{m}$ ), C ( $E_F=0.84\ \text{eV}$  and  $L=1.19\ \mu\text{m}$ ), and D ( $E_F=0.84\ \text{eV}$  and  $L=2.41\ \mu\text{m}$ ). The near-field for peak B ( $E_F=0.64\ \text{eV}$  and  $L=0.97\ \mu\text{m}$ ) can be found in Fig. 5c.

when  $h$  is small enough (in the case of Fig. 6a,  $h < 2.13\ \mu\text{m}$ ). Thus, we need to balance the confinement and the intensity of the field, when we try to design the system. Another interesting feature is that the intensity distribution for the complete absorption case shown in Fig. 7a is different from the one shown in Fig. 7b. This is because the intensity has two contributions, the  $x$ - and  $z$ -components of the electric field. The  $x$ -component contribution is dominated by the vertical Fabry–Pérot effect, while the  $z$ -component contribution is dominated by the horizontal Fabry–Pérot effect. In Fig. 7a, both contributions are strong, which can be clearly seen in Fig. 6c and f. However, in Fig. 7b the  $z$ -component contribution dominates the intensity. Interestingly, the energy in Fig. 7b is mainly trapped in the cavity.

### 3.5. Electrostatic tuning of the graphene plasmons

Plasmonic modes are particularly appealing in graphene due to the ultra-broad and fast tunability of the Fermi energy via chemical doping or electrical doping. Optical gaps of up to 2 eV (which corresponds to  $E_F \sim 1\ \text{eV}$ ) can be achieved [49]. Thus, the peak positions in the absorption spectra can be tuned by electrical or chemical doping. Fig. 8a shows graphene absorption with different Fermi energies for a normal TM incidence. Fig. 8a shows the trench length corresponding to each peak increases with the increase of the Fermi energy. This is because the GP wavelength goes up as the Fermi energy rises. This paves the way to build cheap, reliable, ultra-fast and highly tunable optical modulators. The predictions from Eq. (1) and the ones from Eq. (7) indicate again that the latter equation reveals the cavity height dependence of the dispersion relation. The near-field plots of  $E_z$  for peaks marked as A–D are given in Fig. 8b–d and Fig. 5c.

### 3.6. Symmetric plasmon modes excited at oblique incidence

The previous discussions only consider the normal TM incidence, where only antisymmetric modes are excited in the cavity. Under a TM polarized source at oblique incidence, it is expected that

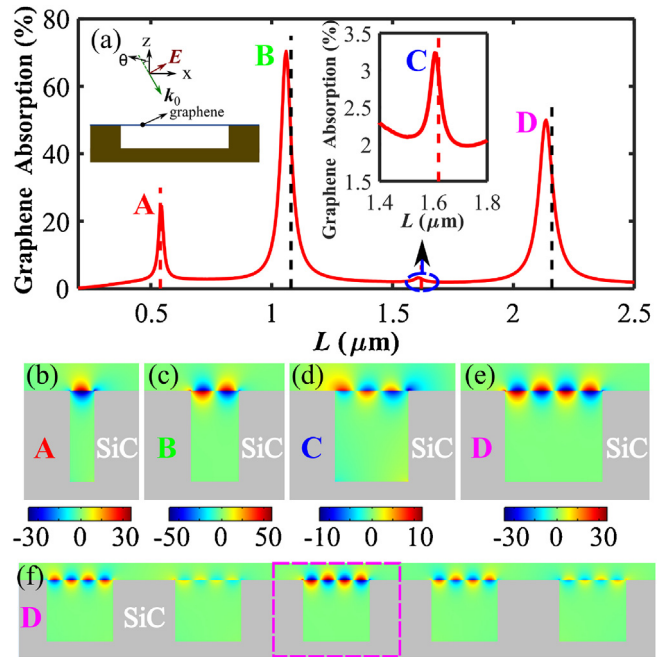


**Fig. 9.** (a) Graphene layer absorption against the trench length ( $L$ ) under a TM polarized oblique incidence at a incident angle of  $\theta=30^\circ$  for fixed geometric parameters  $\lambda_0=12\ \mu\text{m}$ ,  $h=2\ \mu\text{m}$ , and  $W=2.0\ \mu\text{m}$ . The insets are the schematic of a configuration with a metallic substrate and a zoom-in plot of the third peak shown by the blue dashed line. Predictions of peak positions obtained from Eq. (7) are indicated by the vertical dashed lines. (b–e) The peaks correspond to standing waves of the GPs as indicated by the near-field plots of  $E_z$  (here normalised to the incident field magnitude) for peaks A ( $L=0.54\ \mu\text{m}$ ), B ( $L=1.06\ \mu\text{m}$ ), C ( $L=1.61\ \mu\text{m}$ ), and D ( $L=2.135\ \mu\text{m}$ ). The peaks predicted by vertical black lines correspond to antisymmetric plasmon modes as shown in (c) and (e), while the ones predicted by red lines correspond to the symmetric plasmon modes as shown in (b) and (d). (f) Near-field plots of  $E_z$  for five grating periods. The pink dashed box showing the position of the plot in (e).

the incident light breaks the symmetry of the system, and consequently stimulates symmetric plasmon standing waves. In Fig. 9, we show the properties of our system under this case for a fixed incident wavelength and fixed geometric parameters. Compared with Fig. 5a, Fig. 9a exhibits additional absorption peaks corresponding to the symmetric plasmonic modes, when the incidence angle is fixed at  $30^\circ$  with varying the trench length. The predictions from Eq. (7) shown as black dashed lines and red dashed lines in Fig. 9a, agree well with the simulation results. The peaks predicted by vertical black lines correspond to antisymmetric plasmon modes confirmed by Fig. 9c and e, while the ones predicted by red lines correspond to the symmetric plasmon modes confirmed by Fig. 9b and d. It is worth noting that the GP modes of different cavities in the same grating structure are out-of-phase due to the oblique incidence, clearly indicated by the near-field of peak D for five grating periods in Fig. 9f.

### 3.7. Comparison between SiC and metallic substrates

The substrate of the configuration we considered previously is SiC, which acts, to a good approximation, as a PEC at the frequencies of interest. However, it is expected that there is still some difference between SiC and the PEC model.

In this part, we study the effects of different substrates by changing the substrate material of the configuration shown in Fig. 10a. In Fig. 10b, we show the graphene absorption of the system with different substrates for fixed incident wavelength and fixed geometric parameters under the normal TM incidence. The results show that the simulations with the PEC model and

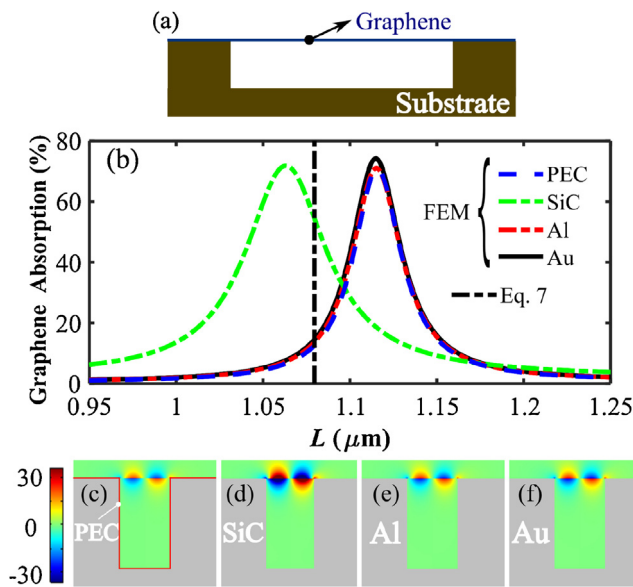


**Fig. 10.** (a) Schematic of a configuration with different substrates. (b) Graphene layer absorption as a function of the grating trench length ( $L$ ) when  $h=2.0\ \mu\text{m}$ ,  $W=2.0\ \mu\text{m}$ , and  $\lambda_0=12\ \mu\text{m}$ . Predictions of peak positions obtained from Eq. (7) are indicated by the vertical black dashed lines. (c–f) The near-field plots of  $E_z$  for different substrates shown in (b). The trench length  $L=1.115\ \mu\text{m}$  is for (c) and (e–f), while  $L=1.063\ \mu\text{m}$  is for (d).

metallic materials (aluminium [50] and gold [51] here) give the qualitatively same behaviour. The behaviour is modified for the system with SiC. This can be understood by viewing the optical properties of SiC and the metallic materials. We find that metallic materials, compared with SiC, acts more like a PEC at the frequencies of interest. It is also worth noting that the whole absorption of the system (not shown) with SiC substrate is much higher than the other three cases. One the other hand, there is a little difference between the prediction from Eq. (7) and the peak position for PEC model. This is because in this work we do not consider the near-field distribution around the sharp edges shown in Fig. 10c. Fig. 10d–f shows the near-field distribution of other cases. Additionally, based on the derived equations in this study, we could predict the most appropriate range of the permittivity for the substrate that may help generate the strongest electric fields on the graphene surface.

### 3.8. Extension toward applications

All scenarios considered until this point are free-standing graphene layer and spaced by air cavities that served to simplify discussion and our understanding of the modes. We consider now simpler and more realistic configurations. First, we fill the cavity with a dielectric medium with the refractive index  $n$ , shown in Fig. 11a, which can be easily achieved by deposition of oxides or an organic layer.

As an example, we analyse the modes exhibited by peak A and peak B shown in Fig. 11b. As expected, the peak positions agree with the predictions from Eq. (7) shown in Fig. 11b, while the predictions obtained from Eq. (1) are not precise. Clearly, there is a small difference between the simulated results from FEM and the predictions from Eq. (7). This is because, although a phase shift of  $-\pi$  is always used to get a fit of Fabry–Pérot model, there should be small difference between the phase shift for different configurations, which can be found by looking at the near-field around the edges. A surprising feature is that the predictions from Eq. (7) remains very good as the number of the peaks increases, while the ones from Eq. (1) become worse. This can be understood by noting that the additional length between peak A and peak B is one GP wavelength (as

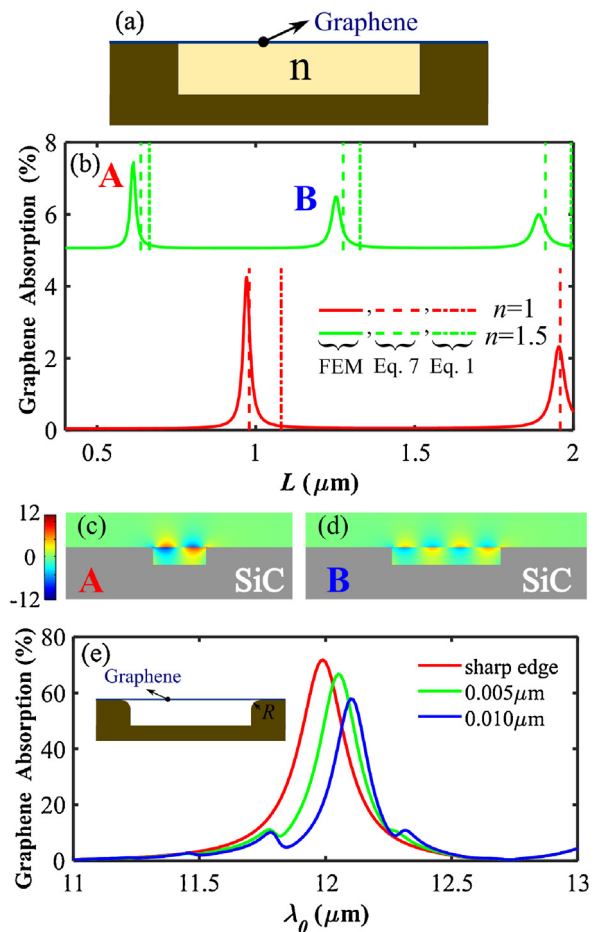


**Fig. 11.** (a) Schematic of a realistic configuration with a dielectric material ( $n$  is its refractive index), filling in the cavity. (b) Graphene layer absorption as a function of the trench length ( $L$ ) of the SiC grating for different values of the refractive index ( $n$ ) of the cavity, when  $h=0.2\ \mu\text{m}$ ,  $W=2.0\ \mu\text{m}$ , and  $\lambda_0=12\ \mu\text{m}$ . Predictions of peak positions obtained from Eq. (7) are indicated by the vertical dashed lines. Predictions from Eq. (1) are also given by the vertical dash-dot lines. The green curve has been offset. (c–d) The near-field plots of  $E_z$  for peaks A ( $L=0.612\ \mu\text{m}$ ) and B ( $L=1.252\ \mu\text{m}$ ) marked in (b). (e) Graphene absorption for different shapes of the cavity edge, when  $L=1.06\ \mu\text{m}$ ,  $h=2.0\ \mu\text{m}$ , and  $W=2.0\ \mu\text{m}$ . The shape of the cavity edge is rounded with radius  $R$  as shown in the inset. The green and blue lines represent results with  $R=0.005\ \mu\text{m}$  and  $R=0.010\ \mu\text{m}$ , respectively. The red line shows the result under the sharp edges of the cavity.

shown in Fig. 11c and d), and the difference between the simulated peak positions and their predictions from Eq. (7) remains the same. This feature is also found in Figs. 5 and 8. This finding confirms the precision of Eq. (7). In addition, by comparing the results under different  $n$  (as shown in Fig. 11b), we find that when the refractive index of the cavity increases, the difference between the results from Eqs. (7) and (1) reduces, and the graphene layer absorption decreases.

Apart from the refractive index of the cavity, the shape of the cavities also has an influence on the graphene surface plasmon. We obtained graphene absorptions under rounded edges of the cavity, as shown in Fig. 11e. The resonances under rounded edges are redshifted with respect to the sharp edges case, and the shift get larger with the increase of the radius  $R$ . This is because the effective trench length increases. Also, new peaks appear due to the different reflection at the edges.

We foresee experimental demonstrations of the existence and manipulation of the cavity modes in such simple geometries. Their extraordinary confinement and strong enhancement could make the system as an ideal interface for sensing and integrated optics.

#### 4. Conclusions

In conclusion, we have analysed the surface plasmon polaritons supported on graphene cavities made of SiC or metallic cavities. An analytical expression for the dispersion relation of GP waves in a multilayer system have been derived. This simple analytical expression is a useful tool showing the cavity height dependence of the dispersion relationship of the GPs. Complete absorption of the system can be achieved under certain parameters, which can be predicted precisely using two Fabry–Pérot models. One Fabry–Pérot model is in the horizontal direction for GPs, while the other one is in the vertical direction for gap SPhPs. The interaction of the SPPs and SPhPs can be used in order to tune the cavity resonances. The tunability of Fermi energy and geometric parameters of the cavities, along with the substrate, make the design of this system very flexible. High enhancement and extraordinary compression of GPs have also been realized under certain conditions. Under oblique incidence, symmetric plasmon modes have been excited. Plasmon cavity modes make this an ideal system for molecular sensing and integrated optics.

#### Conflict of interest

No conflicts of interest are declared by the authors.

#### Acknowledgements

X.X. is supported by Lee Family Scholars. S.M. acknowledges the Lee-Lucas Chair in Physics and the EPSRC Mathematical Fundamentals of Metamaterials Programme Grant (EP/L024926/1) and V.G. is acknowledging ONR Global funding (N62909-15-1-N082).

#### References

- [1] S.A. Maier, M.L. Brongersma, P.G. Kik, S. Meltzer, A.A.G. Requicha, H.A. Atwater, Plasmonics – a route to nanoscale optical devices, *Adv. Mater.* 13 (19) (2001) 1501–1505.
- [2] S.A. Maier, *Plasmonics: Fundamentals and Applications*, Springer Science & Business Media, 2007.
- [3] W.L. Barnes, A. Dereux, T.W. Ebbesen, Surface plasmon subwavelength optics, *Nature* 424 (6950) (2003) 824.
- [4] D.K. Gramotnev, S.I. Bozhevolnyi, Plasmonics beyond the diffraction limit, *Nat. Photon.* 4 (2) (2010) 83–91.
- [5] M. Konig, M. Rahmani, L. Zhang, D.Y. Lei, T.R. Roschuk, V. Giannini, C.-W. Qiu, M. Hong, S. Schlucker, S.A. Maier, Unveiling the correlation between nanometer-thick molecular monolayer sensitivity and near-field enhancement and localization in coupled plasmonic oligomers, *ACS Nano* 8 (9) (2014) 9188–9198.
- [6] K.S. Novoselov, A.K. Geim, S.V. Morozov, D. Jiang, Y. Zhang, S.V. Dubonos, I.V. Grigorieva, A.A. Firsov, Electric field effect in atomically thin carbon films, *Science* 306 (5696) (2004) 666–669.
- [7] F.J.G. de Abajo, Graphene plasmonics: challenges and opportunities, *ACS Photon.* 1 (3) (2014) 135–152.
- [8] C. Zhu, D. Du, Y. Lin, Graphene and graphene-like 2d materials for optical biosensing and bioimaging: a review, *2D Mater.* 2 (3) (2015) 032004.
- [9] K.F. Mak, J. Shan, Photonics and optoelectronics of 2d semiconductor transition metal dichalcogenides, *Nat. Photon.* 10 (4) (2016) 216–226.
- [10] F.H.L. Koppens, D.E. Chang, F.J. García de Abajo, Graphene plasmonics: a platform for strong light-matter interactions, *Nano Lett.* 11 (8) (2011) 3370–3377.
- [11] A.N. Grigorenko, M. Polini, K.S. Novoselov, Graphene plasmonics, *Nat. Photon.* 6 (11) (2012) 749–758.
- [12] L. Ju, B.S. Geng, J. Horng, C. Girit, M. Martin, Z. Hao, H.A. Bechtel, X.G. Liang, A. Zettl, Y.R. Shen, F. Wang, Graphene plasmonics for tunable terahertz metamaterials, *Nat. Nanotechnol.* 6 (10) (2011) 630–634.
- [13] H. Zhang, Ultrathin two-dimensional nanomaterials, *ACS Nano* 9 (10) (2015) 9451–9469.
- [14] Y. Francescato, V. Giannini, S.A. Maier, Strongly confined gap plasmon modes in graphene sandwiches and graphene-on-silicon, *N. J. Phys.* 15 (6) (2013) 063020.
- [15] A.M. Gilbertson, Y. Francescato, T. Roschuk, V. Shautsova, Y. Chen, T.P.H. Sidiropoulos, M. Hong, V. Giannini, S.A. Maier, L.F. Cohen, et al., Plasmon-induced optical anisotropy in hybrid graphene-metal nanoparticle systems, *Nano Lett.* 15 (5) (2015) 3458–3464.
- [16] P. Tassin, T. Koschny, C.M. Soukoulis, Graphene for terahertz applications, *Science* 341 (6146) (2013) 620–621.
- [17] T. Low, P. Avouris, Graphene plasmonics for terahertz to mid-infrared applications, *ACS Nano* 8 (2) (2014) 1086–1101.
- [18] S. Xiao, X. Zhu, B.-H. Li, N. Asger Mortensen, Graphene-plasmon polaritons: From fundamental properties to potential applications, *Front. Phys.* 11 (2) (2016) 117801.
- [19] T. Low, A. Chaves, J.D. Caldwell, A. Kumar, N.X. Fang, P. Avouris, T.F. Heinz, F. Guinea, L. Martin-Moreno, F. Koppens, Polaritons in layered two-dimensional materials, *Nat. Mater.* 16 (2) (2017) 182–194.
- [20] M. Jablan, H. Buljan, M. Soljačić, Plasmonics in graphene at infrared frequencies, *Phys. Rev. B* 80 (24) (2009) 245435.
- [21] V.W. Brar, M.S. Jang, M. Sherrott, J.J. Lopez, H.A. Atwater, Highly confined tunable mid-infrared plasmonics in graphene nanoresonators, *Nano Lett.* 13 (6) (2013) 2541–2547.
- [22] Y. Francescato, V. Giannini, J. Yang, M. Huang, S.A. Maier, Graphene sandwiches as a platform for broadband molecular spectroscopy, *ACS Photon.* 1 (5) (2014) 437–443.
- [23] W. Gao, J. Shu, C. Qiu, Q. Xu, Excitation of plasmonic waves in graphene by guided-mode resonances, *ACS Nano* 6 (9) (2012) 7806–7813.
- [24] T.M. Slipchenko, M.L. Nesterov, L. Martin-Moreno, A. Yu Nikitin, Analytical solution for the diffraction of an electromagnetic wave by a graphene grating, *J. Opt.* 15 (11) (2013) 114008.
- [25] B. Zhao, Z.M. Zhang, Strong plasmonic coupling between graphene ribbon array and metal gratings, *ACS Photon.* 2 (11) (2015) 1611–1618.
- [26] K. Li, J.M. Fitzgerald, X. Xiao, J.D. Caldwell, C. Zhang, S.A. Maier, X. Li, V. Giannini, Graphene plasmon cavities made with silicon carbide, *ACS Omega* 2 (7) (2017) 3640–3646.
- [27] J.N. Chen, M. Badioli, P. Alonso-Gonzalez, S. Thongrattanasiri, F. Huth, J. Osmond, M. Spasenovic, A. Centeno, A. Pesquera, P. Godignon, A.Z. Elorza, N. Camara, F.J.G. de Abajo, R. Hillenbrand, F.H.L. Koppens, Optical nano-imaging of gate-tunable graphene plasmons, *Nature* 487 (7405) (2012) 77–81.
- [28] Z. Fei, A.S. Rodin, G.O. Andreev, W. Bao, A.S. McLeod, M. Wagner, L.M. Zhang, Z. Zhao, M. Thiemens, G. Dominguez, M.M. Fogler, A.H. Castro Neto, C.N. Lau, F. Keilmann, D.N. Basov, Gate-tuning of graphene plasmons revealed by infrared nano-imaging, *Nature* 487 (7405) (2012) 82–85.
- [29] A. Woessner, M.B. Lundeberg, Y. Gao, A. Principi, P. Alonso-González, M. Carrega, K. Watanabe, T. Taniguchi, G. Vignale, M. Polini, J. Hone, R. Hillenbrand, F.H.L. Koppens, Highly confined low-loss plasmons in graphene-boron nitride heterostructures, *Nat. Mater.* 14 (4) (2014) 421–425.
- [30] J. Chen, M.L. Nesterov, A.Y. Nikitin, S. Thongrattanasiri, P. Alonso-Gonzalez, T.M. Slipchenko, F. Speck, M. Ostler, T. Seyller, I. Crassee, et al., Strong plasmon reflection at nanometer-size gaps in monolayer graphene on sic, *Nano Lett.* 13 (12) (2013) 6210–6215.
- [31] P. Alonso-Gonzalez, A.Y. Nikitin, F. Golmar, A. Centeno, A. Pesquera, S. Velez, J. Chen, G. Navickaite, F. Koppens, A. Zurutuza, F. Casanova, L.E. Hueso, R. Hillenbrand, Controlling graphene plasmons with resonant metal antennas and spatial conductivity patterns, *Science* 344 (June (6190)) (2014) 1369–1373.
- [32] S. Shen, A. Narayanaswamy, G. Chen, Surface phonon polaritons mediated energy transfer between nanoscale gaps, *Nano Lett.* 9 (8) (2009) 2909–2913.
- [33] J.D. Caldwell, L. Lindsay, V. Giannini, I. Vurgaftman, T.L. Reinecke, S.A. Maier, O.J. Glembocki, Low-loss, infrared and terahertz nanophotonics using surface phonon polaritons, *Nanophotonics* 4 (1) (2015) 44–68.
- [34] T. Taubner, D. Korobkin, Y. Urzhumov, G. Shvets, R. Hillenbrand, Near-field microscopy through a sic superlens, *Science* 313 (5793) (2006) 1595.
- [35] J.D. Caldwell, O.J. Glembocki, Y. Francescato, N. Sharav, V. Giannini, F.J. Bezares, J.P. Long, J.C. Owrutsky, I. Vurgaftman, J.G. Tischler, et al., Low-loss, extreme subdiffraction photon confinement via silicon carbide localized surface phonon polariton resonators, *Nano Lett.* 13 (8) (2013) 3690–3697.
- [36] R. Hillenbrand, T. Taubner, F. Keilmann, Phonon-enhanced light-matter interaction at the nanometre scale, *Nature* 418 (6894) (2002) 159.
- [37] Y. Chen, Y. Francescato, J.D. Caldwell, V. Giannini, T.W.W. Maß, O.J. Glembocki, F.J. Bezares, T. Taubner, R. Kasica, M. Hong, et al., Spectral tuning of localized surface phonon polariton resonators for low-loss mid-ir applications, *ACS Photon.* 1 (8) (2014) 718–724.
- [38] B.T. Spann, R. Compton, D. Ratchford, J.P. Long, A.D. Dunkelberger, P.B. Klein, A.J. Giles, J.D. Caldwell, J.C. Owrutsky, Photoinduced tunability of the reststrahlen band in 4H-SiC, *Phys. Rev. B* 93 (8) (2016) 085205.
- [39] A.D. Dunkelberger, C.T. Ellis, D.C. Ratchford, A.J. Giles, M. Kim, C.S. Kim, B.T. Spann, I. Vurgaftman, J.G. Tischler, J.P. Long, et al., Active tuning of surface phonon polariton resonances via carrier photoinjection, *Nat. Photon.* 12 (1) (2018) 50.
- [40] P. Li, X. Yang, T.W.W. Maß, J. Hanss, M. Lewin, A.-K.U. Michel, M. Wuttig, T. Taubner, Reversible optical switching of highly confined phonon-polaritons with an ultrathin phase-change material, *Nat. Mater.* 15 (8) (2016) 870.
- [41] E.H. Hwang, S. Das Sarma, Dielectric function, screening, and plasmons in two-dimensional graphene, *Phys. Rev. B* 75 (20) (2007) 205418.
- [42] S. Thongrattanasiri, A. Manjavacas, F. Javier García de Abajo, Quantum finite-size effects in graphene plasmons, *ACS Nano* 6 (2) (2012) 1766–1775.
- [43] Y. Francescato, New frequencies and geometries for plasmonics and metamaterials, (PhD thesis), Imperial College London, 2014.

- [44] D. Woolf, M. Loncar, F. Capasso, The forces from coupled surface plasmon polaritons in planar waveguides, *Opt. Express* 17 (22) (2009) 19996–20011.
- [45] V. Giannini, Y. Zhang, M. Forcales, J. Gómez Rivas, Long-range surface polaritons in ultra-thin films of silicon, *Opt. Express* 16 (24) (2008) 19674–19685.
- [46] J. Gómez Rivas, G. Vecchi, V. Giannini, Surface plasmon polariton-mediated enhancement of the emission of dye molecules on metallic gratings, *N. J. Phys.* 10 (10) (2008) 105007.
- [47] C.L.C. Smith, N. Stenger, A. Kristensen, N. Asger Mortensen, S.I. Bozhevolnyi, Gap and channeled plasmons in tapered grooves: a review, *Nanoscale* 7 (21) (2015) 9355–9386.
- [48] J.R. Piper, S. Fan, Total absorption in a graphene monolayer in the optical regime by critical coupling with a photonic crystal guided resonance, *ACS Photon.* 1 (4) (2014) 347–353.
- [49] C.F. Chen, C.H. Park, B.W. Boudouris, J. Horng, B.S. Geng, C. Girit, A. Zettl, M.F. Crommie, R.A. Segalman, S.G. Louie, F. Wang, Controlling inelastic light scattering quantum pathways in graphene, *Nature* 471 (7340) (2011) 617–620.
- [50] A.D. Rakić, Algorithm for the determination of intrinsic optical constants of metal films: application to aluminum, *Appl. Opt.* 34 (22) (1995) 4755–4767.
- [51] S. Babar, J.H. Weaver, Optical constants of Cu, Ag, and Au revisited, *Appl. Opt.* 54 (3) (2015) 477–481.